



Long-range intercellular Ca^{2+} wave patterns



C.B. Tabi^{a,b,c,d,*}, I. Maïna^a, A. Mohamadou^e, H.P.F. Ekobena^a, T.C. Kofané^f

^a Laboratory of Biophysics, Department of Physics, Faculty of Science, University of Yaoundé I, P.O. Box 812, Yaoundé, Cameroon

^b Institute of Theoretical Physics, Department of Physics, Faculty of Science, University of Stellenbosch, Private Bag X1 Matieland, Stellenbosch 7602, South Africa

^c The African Institute for Mathematical Sciences, 6-8 Melrose Rd, Muizenberg 7945, South Africa

^d Institute of Theoretical and Computational Physics, Department of Physics, College of Sciences, Botswana International University of Science and Technology, Private Mail Bag 16 Palapye, Botswana

^e Department of Physics, Faculty of Science, University of Maroua, P.O. Box 46, Maroua, Cameroon

^f Laboratory of Mechanics, Department of Physics, Faculty of Science, University of Yaoundé I, P.O. Box 812, Yaoundé, Cameroon

HIGHLIGHTS

- Effect of long-range interaction is studied in a discrete cell network.
- Modulational instability is studied both analytically and numerically.
- Extended breather-like structures are obtained for perfect intercellular communication.
- High range parameter kills long-range modulated calcium waves.

ARTICLE INFO

Article history:

Received 8 January 2015

Received in revised form 27 March 2015

Available online 30 April 2015

Keywords:

Cell–cell communication

Long-range interaction

Patterns

Solitons

ABSTRACT

Modulational instability is utilized to investigate intercellular Ca^{2+} wave propagation in an array of diffusively coupled cells. Cells are supposed to be connected via paracrine signaling, where long-range effects, due to the presence of extracellular messengers, are included. The multiple-scale expansion is used to show that the whole dynamics of Ca^{2+} waves, from the endoplasmic reticulum to the cytosol, can be reduced to a single differential-difference nonlinear equation whose solutions are assumed to be plane waves. Their linear stability analysis is studied, with emphasis on the impact of long-range coupling, via the range parameter s . It is shown that s , as well as the number of interacting cells, importantly modifies the features of modulational instability, as small values of s imply a strong coupling, and increasing its value rather reduces the problem to a first-neighbor one. Our theoretical findings are numerically tested, as the generic equations are fully integrated, leading to the emergence of nonlinear patterns of Ca^{2+} waves. Strong long-range coupling is pictured by extended trains of breather-like structures whose frequency decreases with increasing s . We also show numerically that the number of interacting cells plays on the spatio-temporal formation of Ca^{2+} patterns, whilst the quasi-perfect intercellular communication depends on the paracrine coupling parameter.

© 2015 Elsevier B.V. All rights reserved.

* Corresponding author at: Laboratory of Biophysics, Department of Physics, Faculty of Science, University of Yaoundé I, P.O. Box 812, Yaoundé, Cameroon. Tel.: +237 6788 735 50.

E-mail addresses: conrad@aims.ac.za, tabi.conrad@uy1.uninet.cm (C.B. Tabi).

1. Introduction

Information processing in animal and vegetal cells is partly ensured by calcium ions (Ca^{2+}), whose complex oscillatory behaviors have been of theoretical, as well as experimental, interest during the last decades. In a wide variety of these cells, cytosolic Ca^{2+} waves (CaWs) are stimulated by extracellular agonists, which provoke the release of Ca^{2+} from the endoplasmic reticulum (ER) to the cytosol. This process which involves a second messenger inositol-1,4,5-triphosphate (IP_3), has been shown to regulate number of cellular functions such as synaptic transmission and muscle contractions [1], and gene expression [2], as a consequence of a transient increase of intracellular Ca^{2+} concentration. Importantly, high cytoplasmic Ca^{2+} concentration can coordinate the activities of neighboring cells [3]. Besides, specific processes such as mucociliary clearance, mechanical transduction, cell growth, just to name a few, are supported by intercellular communications. The importance of the mechanism CaW spreading among neighboring cells is therefore raised, as compelling data show gap junction and paracrine signaling to be the most popular. While gap junctions are made of transmembrane channels between two adjacent cells, thus allowing diffusing exchange of nutrients between them [4–6], paracrine coupling is rather guaranteed by signaling molecules, released by one cell, which diffuses in the extracellular medium and binds to membrane receptors of neighboring cells [7]. Although the two mechanisms are sometimes differentiated, it is not to be ignored that in many cells, they act simultaneously to efficiently coordinate and integrate information between cells. However, intercellular waves relying exclusively on IP_3 diffusion through gap junctions spread on reduced distances, whereas CaWs relying on paracrine signaling can spread over long distances, therefore suggesting the hypothesis of long-range interaction (LRI) among coupled cells, which is the main concern of the present work. Substantial investigations on the way cells exchange information have led to the elaboration of interesting mathematical models among which the one by Sneyd [8], related to mechanically induced waves, with recent improvement applied to intercellular coupling in hepatocytes [9]. The same model has been employed by Gracheva and Gunton [10] and the concept of intercellular communication via gap junctions has been reinforced as mediated by messengers such as Ca^{2+} and IP_3 . However, all the models addressed in these contributions are continuum, whereas cells, in arrays, could be pictured as discrete entity with effective nearest-neighbor interactions [11,12]. This other aspect of the problem has been studied recently, yielding the conclusion that the discrete model could better describe spreading of pathologies via abnormal Ca^{2+} oscillations from an infected cell to the whole lattice [11,12]. However, in Ref. [12] Tabi et al., exclusively making use of the modulational instability (MI) technique, have shown that the discrete model, with paracrine signaling, was quite interesting in describing and characterizing quasi-perfect intercellular communication. To remind, the MI phenomenon in a direct mechanism that is at the basis of solitons and pattern formation in systems where the concomitant effects of dispersion and nonlinearity are effective [13]. The technique has been deeply applied to different physical setting from various areas of physics such nonlinear optics [14], hydrodynamics [15], biophysics [16–19] and Bose–Einstein condensates [20], just to name a few.

In real situations, where the extracellular messengers can be propagating throughout the extracellular fluid, connecting nearest- as well as non-nearest-neighbor cells [21–23], as stated so far, it would be of importance to think of long-range coupling among the cells forming the network. As in Ref. [12], the MI analysis will also be used. In Section 2, we introduce the modified discrete model for intercellular CaWs and we use the multiple scaling expansion to show that the ER and cytosolic calcium dynamics can be reduced to a single differential-difference nonlinear equation. In Section 3, the linear stability analysis of a plane wave, solution of the latter, will be performed and the stability/instability features will be discussed. In the same section, numerical simulations, to verify our analytical predictions, will be carried out from the generic equations. The last section will be devoted to some concluding remarks.

2. Model and asymptotic expansion

2.1. The model

Realistically, two aspects must be considered in the study of intercellular CaWs dynamics among coupled cells: the intracellular dynamics of Ca^{2+} and its spreading throughout the network. The minimal model by Goldbeter et al. [24] can be adopted as it suggests that stimulation of neighboring cells is due to Ca^{2+} extruded from one cell. Explicitly, we assume a one-dimensional cell network as the one shown in Fig. 1, whose experimental evidences are supported by the way acrasial amoeba come together and form thin multicellular rods when life conditions become unfavorable [25]. They can share nutrients and information as they couple through a substance known as acrasin. Mathematically, the model we are proposing here couples Ca^{2+} concentrations both in the cytosol, x_n , and in the ER, y_n , of the n th cell as follows:

$$\frac{dx_n}{dt} = a_n + \sum_{m \neq n} k_{nm}(x_m - x_n) - V_{2,n} + V_{3,n} + k_f y_n - k x_n \quad (1a)$$

$$\frac{dy_n}{dt} = V_{2,n} - V_{3,n} - k_f y_n. \quad (1b)$$

In comparison to the model of Ref. [12], the present model is generalized via the presence of the term $\sum_{m \neq n} k_{nm}(x_m - x_n)$ which characterizes long-range diffusive interaction. The latter is due to the fact that the extracellular messenger can

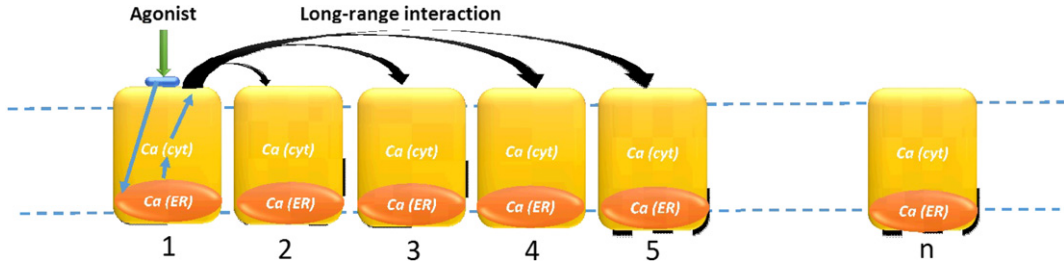


Fig. 1. Schematic representation of the long-range intercellular communication via paracrine signaling. In general, the process is initiated by an agonist that binds to the cell membrane then exciting the internal Ca^{2+} store, the ER, leading to the release of Ca^{2+} from the ER to the cytosol. Large black arrows picture the process of cell–cell communication.

propagate from one cell to its direct neighbors via extracellular fluid and even extend to other neighboring non-contacting cells as indicated by the black arrows of Fig. 1. The coupling constant has a power-law dependence as

$$k_{nm} = \beta V_1 |n - m|^{-s}, \quad (2)$$

with βV_1 being the paracrine coupling parameter, while the long-range interaction is regulated by the parameter $1 \leq s < \infty$. We should however stress that for $s \rightarrow +\infty$, the problem is reduced to the nearest-neighbor interactions. In Fig. 2, we have, for example, plotted the coupling constant k_{nm} versus the absolute value of the distance between the two cells, $|n - m|$. It is then clear that the LRI is stronger for small values of s , while it is restricted to $|n - m| = 1$ for $s = 20$. The term

$$V_{2,n} = \frac{V_{m2} x_n^2}{k_2^2 + x_n^2} \quad (3)$$

represents the rate of Ca^{2+} from the cytosol to the ER, while the term

$$V_{3,n} = \frac{V_{m3} x_n^4 y_n^2}{(k_a^4 + x_n^4)(k_r^2 + y_n^2)} \quad (4)$$

stands for the rate of Ca^{2+} release from the ER to the cytosol. In Eq. (1a), the presence of the agonist is materialized by the term

$$a_n = \begin{cases} V_0 + bV_1, & \text{if } n = 1 \\ V_0, & \text{elsewhere} \end{cases} \quad (5)$$

with V_0 being the influx of Ca^{2+} from the extracellular media and the term bV_1 , the constant hormonal stimulus occurring in the first cell of the lattice. In the absence of external stimulation, i.e., $b = 0$, the influx and flux of Ca^{2+} will still be effective thanks to the terms V_0 and kx_n . More clearly, the Ca^{2+} extrusion from cytosol to the extracellular medium is modeled by the term kx_n , and the term $k_f y_n$ implies that Ca^{2+} can move from the ER to the cytosol and vice-versa. In the rest of the paper, we will consider $j = m - n$ and $k_0 = \beta V_1$. We consider in general an infinite number of identical cells, but as the signal can be reproduced after a given number M of cells, we restrict ourselves in the rest of this work, mainly for the numerical analysis, to $M = 500$ which allows us to use periodic boundary conditions. In order to efficiently apply the asymptotic expansion, we propose to further simplify the above equations, keeping up to the third-order terms in x_n and y_n as follows:

$$\begin{aligned} \frac{dx_n}{dt} = & \left(\frac{V_0}{k_2^2} - \alpha_3 \right) x_n^2 + \frac{V_0}{k_r^2} y_n^2 + \sum_{j=1}^{\infty} k_0 |j|^{-s} \left[1 + \alpha_1 y_n^2 + \alpha_2 x_n^2 \right] (x_{n+j} + x_{n-j} - 2x_n) \\ & + k_f y_n - \gamma_2 x_n y_n^2 + \beta_2 y_n x_n^2 - \gamma_1 x_n^3 + \beta_1 y_n^3 - kx_n \end{aligned} \quad (6a)$$

$$\frac{dy_n}{dt} = \alpha_3 x_n^2 - k_f y_n - \beta_2 y_n x_n^2 - \beta_1 y_n^3, \quad (6b)$$

where we have assumed all the cells to receive the identical influx of Ca^{2+} from the extracellular media, i.e., $b = 0$ and $V_0 \neq 0$, only for analytical manipulations. We have also introduced the parameters $\alpha_1 = \frac{1}{k_r^2}$, $\alpha_2 = \frac{1}{k_2^2}$, $\alpha_3 = \frac{V_{m2}}{k_2^2}$, $\gamma_2 = \frac{k}{k_r^2}$,

$$\beta_2 = \frac{k_f}{k_2^2}, \gamma_1 = \frac{k}{k_2^2} \text{ and } \beta_1 = \frac{k_f}{k_r^2}.$$

2.2. The amplitude equation

The multiple-scale expansion is an asymptotic expansion method in which both the amplitude and the carrier wave are considered to be discrete, the main objective being to obtain more manipulable amplitude equations. This has been recently

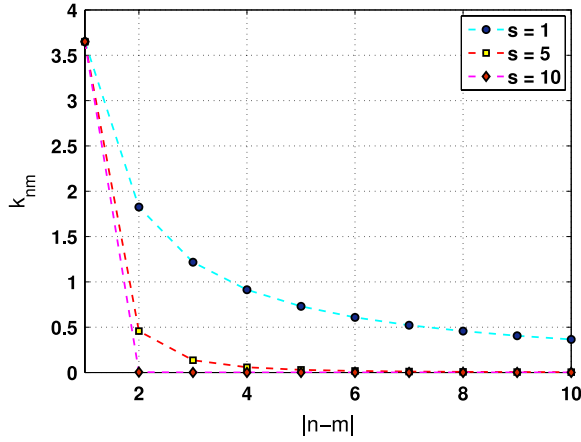


Fig. 2. The coupling between cells n and m is ensured via the coupling parameter k_{nm} , which depends on the absolute value of the distance between the two cells, $|n - m|$. k_{nm} is plotted versus $|n - m|$ for different values of the range parameter s . Small values of s imply a strong long-range coupling ($s = 1$), while increasing s , i.e., $s = 5$ and $s = 10$, reduces interactions to the first nearest-neighbors.

possible in electrical lattices [26], as well as in biological systems [12,18,27]. In this section, we employ the same method to investigate the amplitude modulation of Ca^{2+} oscillations via Eqs. (6). We proceed by assuming that generalized solutions for system (6) are given by the Fourier transforms

$$x_n(t) = \int d\omega \hat{\psi}(\omega) e^{i(\omega t + q_0 n)} \quad \text{and} \quad y_n(t) = \int d\omega \hat{\phi}(\omega) e^{i(\omega t + q_0 n)}, \quad (7)$$

where, because of nonlinear effects, the frequency ω and the wavenumber q_0 undergo deviations as $\omega = \Omega + \epsilon\lambda$, $q_0 = q + \epsilon \frac{\lambda}{v_g} + \epsilon^2 c_g \lambda^2 + \dots$, with $v_g = \frac{\partial \Omega}{\partial q}$, the group velocity and $2c_g = \frac{\partial^2 \Omega}{\partial q^2}$, the group velocity dispersion, λ being a small deviation from the natural frequency Ω . To further simplicity, we fix $c_g = 1$, and ansatz (7) reduce to

$$\begin{aligned} x_n(t) &= e^{i(\Omega t + qn)} \left(\epsilon \int d\lambda \hat{\psi}(\lambda) e^{i\epsilon\lambda \left(t + \frac{n}{v_g}\right)} e^{i\lambda^2 \epsilon^2 n} \right), \\ y_n(t) &= e^{i(\Omega t + qn)} \left(\epsilon \int d\lambda \hat{\phi}(\lambda) e^{i\epsilon\lambda \left(t + \frac{n}{v_g}\right)} e^{i\lambda^2 \epsilon^2 n} \right). \end{aligned} \quad (8)$$

From (8), the change of variables $\tau_n = \epsilon(t + n/v_g)$, $\xi_n = \epsilon^2 n$ can be easily introduced, and the expressions for the wave packets become

$$x_n(t) = A(n, t) \psi(\xi_n, \tau_n) \quad \text{and} \quad y_n(t) = A(n, t) \phi(\xi_n, \tau_n), \quad (9)$$

where $A(n, t) = e^{i(qn + \Omega t)}$ and

$$\begin{aligned} \psi(\xi_n, \tau_n) &= \epsilon \int d\lambda \hat{\psi}(\lambda) e^{i(\lambda \tau_n + \lambda^2 \xi_n)} \\ \phi(\xi_n, \tau_n) &= \epsilon \int d\lambda \hat{\phi}(\lambda) e^{i(\lambda \tau_n + \lambda^2 \xi_n)}. \end{aligned} \quad (10)$$

Since discreteness effects are pronounced in the studied model, the small parameter can be taken as $\epsilon^2 = 1/N$. On this background, a large grid for a slow variable m can be constructed by sampling the original grid at each $N = \epsilon^{-2}$, the closest odd integer. Therefore, we can index ξ_n by m , so that $\dots, (n-N) \rightarrow (m-1), n \rightarrow m, (n+N) \rightarrow (m+1), \dots$. More precisely,

$$\dots, \xi_{n-N} = (m-1), \quad \xi_n = m, \quad \xi_{n+N} = (m+1), \quad \dots \quad (11)$$

All the above otherwise implies that the slow modulations $\psi(\xi_n, \tau_n)$ and $\phi(\xi_n, \tau_n)$ of the plane wave $A(n, t)$ can be respectively replaced by the functions $\psi(m, \tau)$ and $\phi(m, \tau)$ of the variables m and $\tau = \tau_n$.

On applying the above scheme, we consider that the trial solutions for system (6) can be regarded as Fourier expansions in harmonics of the fundamental $A^{(l)}(n, t) = e^{il(qn + \Omega t)}$, where the Fourier components are developed in a Taylor's series in powers of the small parameter ϵ . The solutions for x_n and y_n can therefore be adopted as

$$x_n = \sum_{p=1}^{p=\infty} \epsilon^p \sum_{l=-p}^{l=p} \psi_p^{(l)}(\xi_n, \tau_n) A^{(l)}(n, t) \quad \text{and} \quad y_n = \sum_{p=1}^{p=\infty} \epsilon^p \sum_{l=-p}^{l=p} \phi_p^{(l)}(\xi_n, \tau_n) A^{(l)}(n, t), \quad (12)$$

with $\psi_p^{(-l)} = \left(\psi_p^{(l)}\right)^*$ and $\phi_p^{(-l)} = \left(\phi_p^{(l)}\right)^*$.

Applying these solutions to Eqs. (6) leads to the set of coupled equations

$$\begin{aligned}
 & \sum_{p=1}^{\infty} \epsilon^p \sum_{l=-p}^p \left(\epsilon \frac{\partial}{\partial \tau} \psi_p^{(l)}(m, \tau) + i l \Omega \psi_p^{(l)}(m, \tau) \right) A^l(n, t) \\
 &= \sum_{p=1}^{\infty} \epsilon^p \sum_{l=-p}^p \sum_{j=1}^{\infty} k_0 |j|^{-s} \left[2(\cos(qjl) - 1) \psi_p^{(l)}(m, \tau) + \epsilon \left(\frac{2ij}{v_g} \right) \sin(qjl) \frac{\partial}{\partial \tau} \psi_p^{(l)}(m, \tau) \right. \\
 &\quad \left. + \epsilon^2 \left(\frac{j}{v_g} \right)^2 \cos(qjl) \frac{\partial^2}{\partial \tau^2} \psi_p^{(l)}(m, \tau) + i \epsilon^2 \sin(qjl) \left(\psi_p^{(l)}(m+j, \tau) - \psi_p^{(l)}(m-j, \tau) \right) \right] A^l(n, t) \\
 &\quad \times \left[1 + \alpha_2 \left(\sum_{p=1}^{\infty} \epsilon^p \sum_{l=-p}^p \psi_p^{(l)}(m, \tau) A^{(l)} \right)^2 + \alpha_1 \left(\sum_{p=1}^{\infty} \epsilon^p \sum_{l=-p}^p \phi_p^{(l)}(m, \tau) A^{(l)} \right)^2 \right] \\
 &\quad + \left(\frac{V_0}{k_2^2} - \alpha_3 \right) \left(\sum_{p=1}^{\infty} \epsilon^p \sum_{l=-p}^p \psi_p^{(l)}(m, \tau) A^{(l)} \right)^2 + k_f \left(\sum_{p=1}^{\infty} \epsilon^p \sum_{l=-p}^p \phi_p^{(l)}(m, \tau) A^{(l)} \right) \\
 &\quad - \gamma_2 \left(\sum_{p=1}^{\infty} \epsilon^p \sum_{l=-p}^p \psi_p^{(l)}(m, \tau) A^{(l)} \right) \left(\sum_{p=1}^{\infty} \epsilon^p \sum_{l=-p}^p \phi_p^{(l)}(m, \tau) A^{(l)} \right)^2 + \frac{V_0}{k_r^2} \left(\sum_{p=1}^{\infty} \epsilon^p \sum_{l=-p}^p \phi_p^{(l)}(m, \tau) A^{(l)} \right)^2 \\
 &\quad + \beta_2 \left(\sum_{p=1}^{\infty} \epsilon^p \sum_{l=-p}^p \phi_p^{(l)}(m, \tau) A^{(l)} \right) \left(\sum_{p=1}^{\infty} \epsilon^p \sum_{l=-p}^p \psi_p^{(l)}(m, \tau) A^{(l)} \right)^2 - \gamma_1 \left(\sum_{p=1}^{\infty} \epsilon^p \sum_{l=-p}^p \psi_p^{(l)}(m, \tau) A^{(l)} \right)^3 \\
 &\quad + \beta_1 \left(\sum_{p=1}^{\infty} \epsilon^p \sum_{l=-p}^p \phi_p^{(l)}(m, \tau) A^{(l)} \right)^3 - k \left(\sum_{p=1}^{\infty} \epsilon^p \sum_{l=-p}^p \psi_p^{(l)}(m, \tau) A^{(l)} \right) \quad (13a)
 \end{aligned}$$

$$\begin{aligned}
 & \sum_{p=1}^{\infty} \epsilon^p \sum_{l=-p}^p \left(\epsilon \frac{\partial}{\partial \tau} \phi_p^{(l)}(m, \tau) + i l \Omega \phi_p^{(l)}(m, \tau) \right) A^l(n, t) \\
 &= \alpha_3 \left(\sum_{p=1}^{\infty} \epsilon^p \sum_{l=-p}^p \psi_p^{(l)}(m, \tau) A^{(l)} \right)^2 - k_f \left(\sum_{p=1}^{\infty} \epsilon^p \sum_{l=-p}^p \phi_p^{(l)}(m, \tau) A^{(l)} \right) \\
 &\quad - \beta_2 \left(\sum_{p=1}^{\infty} \epsilon^p \sum_{l=-p}^p \phi_p^{(l)}(m, \tau) A^{(l)} \right) \left(\sum_{p=1}^{\infty} \epsilon^p \sum_{l=-p}^p \psi_p^{(l)}(m, \tau) A^{(l)} \right)^2 - \beta_1 \left(\sum_{p=1}^{\infty} \epsilon^p \sum_{l=-p}^p \phi_p^{(l)}(m, \tau) A^{(l)} \right)^3, \quad (13b)
 \end{aligned}$$

that we intend to solve by considering the different orders of the small parameter ϵ . In this framework, the leading order (1, l) is governed by the homogeneous system in $\psi_1^{(l)}$ and $\phi_1^{(l)}$ (Appendix A), which, for $l = 0$, has the solutions

$$\psi_1^{(0)}(m, \tau) = \phi_1^{(0)}(m, \tau) = 0. \quad (14)$$

The case $l = 1$ leads to the homogeneous system in $\psi_1^{(1)}$ and $\phi_1^{(1)}$, which admits non-trivial solutions if its determinant is null, given that the dispersion relation

$$\left(i\Omega - 2 \sum_{j=1}^{\infty} k_0 |j|^{-s} (\cos(qj) - 1) + k \right) (i\Omega + k_f) = 0 \quad (15)$$

is satisfied. The latter leads to the solutions

$$\psi_1^{(1)} = \eta(m, \tau) \quad \text{and} \quad \phi_1^{(1)} = 0. \quad (16)$$

We now consider the order (2, l), which is also governed by a set of coupled equations in $\psi_2^{(l)}$ and $\phi_2^{(l)}$, given in Appendix B, where the case $l = 0$ gives the solutions

$$\psi_2^{(0)} = \frac{V_0}{kk_2^2} |\eta(m, \tau)|^2 \quad \text{and} \quad \phi_2^{(0)} = \frac{2\alpha_3}{k_f} |\eta(m, \tau)|^2. \quad (17)$$

Along the same line, for $l = 1$, the set of equations for $\psi_2^{(1)}$ and $\phi_2^{(1)}$ is obtained, and the compatibility condition gives the group velocity $v_g = \frac{\partial \Omega}{\partial q} = 2i \sum_{j=1}^{\infty} k_0 |j|^{1-s} \sin(qj)$, while the solutions are such that

$$\psi_2^{(1)} = \chi(m, \tau) \quad \text{and} \quad \phi_2^{(1)} = 0. \quad (18)$$

Still for $p = 2$, we consider $l = 2$ and we obtain a set of equations whose solutions are

$$\psi_2^{(2)} = \frac{\frac{k_f \alpha_3}{2i\Omega + k_f} + \frac{V_0}{k_2^2} - \alpha_3}{2i\Omega + k - 2 \sum_{j=1}^{\infty} k_0 |j|^{-s} (\cos(2qj) - 1)} (\eta(m, \tau))^2 \quad \text{and} \quad \phi_2^{(2)} = \frac{\alpha_3}{2i\Omega + k_f} (\eta(m, \tau))^2. \quad (19)$$

Finally, we solve the system for $\psi_3^{(1)}$ and $\phi_3^{(1)}$, which is obtained for $p = 3$ and $l = 1$ (see [Appendix C](#)), and yields, after making use of the previous solutions, the amplitude equation in $\eta(m, \tau) = \eta_m(\tau)$ as follows:

$$i \sum_j P_j (\eta_{m+j} - \eta_{m-j}) + Q \frac{\partial^2}{\partial \tau^2} \eta_m + R |\eta_m|^2 \eta_m = 0, \quad (20)$$

where the q -dependent parameters P_j , Q and R are given by

$$P_j = k_0 |j|^{-s} \sin(qj) \quad Q = -\frac{1}{4k_0} \times \frac{\sum_{j=1}^{\infty} |j|^{2-s} \cos(qj)}{\left(\sum_{j=1}^{\infty} |j|^{1-s} \sin(qj) \right)^2} \quad (21)$$

$$R = -12\alpha_2 k_0 \sum_{j=1}^{\infty} |j|^{-s} \sin^2\left(\frac{qj}{2}\right) - 3\gamma_1 + \left(\delta + \frac{V_0}{kk_2^2} \right) \left\{ 2 \left(\frac{V_0}{k_2^2} - \alpha_3 \right) + \frac{2\alpha_3 k_f}{k_f - k - 4k_0 \sum_{j=1}^{\infty} |j|^{-s} \sin^2\left(\frac{qj}{2}\right)} \right\},$$

with

$$\delta = \frac{\frac{\alpha_3 k_f}{k_f - 2k - 8k_0 \sum_{j=1}^{\infty} |j|^{-s} \sin^2\left(\frac{qj}{2}\right)} + \frac{V_0}{k_2^2} - \alpha_3}{4k_0 \sum_{j=1}^{\infty} |j|^{-s} \sin^2(qj) - 4k_0 \sum_{j=1}^{\infty} |j|^{-s} \sin^2\left(\frac{qj}{2}\right) - k}.$$

The global form of Eq. (20) has already been obtained in electrical transmission lines [26], and in some biological systems such as DNA nonlinear dynamics [16], calcium dynamics in coupled cells [12], blood flow [18], just to name a few. However, in these systems, long-range dispersive interactions have not been taken into consideration, and the sum that appears in the first terms of that equation simply describes long-range coupling. Eq. (20) will therefore be used to study the linear stability analysis, while direct numerical simulations will be done with the set of Eqs. (1), with the parameters of [Table 1](#) which correspond to oscillation features of the Goldbeter–Dupont–Berridge (GDB) model [24].

3. Unstable Ca^{2+} patterns

3.1. Linear stability analysis

To study the linear stability analysis of a plane wave, we introduce a slight perturbation in the amplitude of the solution. Therefore, we introduce the solution $\eta_m(\tau) = \text{Be}^{i(\lambda m - \mu \tau)}$ into Eq. (20), the wavenumber λ and the frequency of perturbation μ being related by the nonlinear dispersion relation

$$\mu^2 = -\frac{R}{Q} \left(\frac{\sum_{j=1}^{\infty} 2k_0 |j|^{-s} \sin(\lambda j) \sin(qj)}{R} + |\eta_0|^2 \right). \quad (22)$$

The plane wave solution will be unstable if $\mu^2 < 0$, which otherwise implies the contribution of the two terms $-R/Q$ and $\frac{2k_0}{R} \sum_{j=1}^{\infty} k_0 |j|^{-s} \sin(\lambda j) \sin(qj) - |\eta_0|^2$. We should however stress that for $j = 1$ the problem reduces to a first nearest-neighbor case which has been discussed in Ref. [12]. However, the present problem is a little bit complicated because of the long-range character of the paracrine signaling. We therefore have to discuss the values of λ for which the MI condition is fulfilled. On this background, we have plotted in [Fig. 3](#) the function $\sin(\lambda j)$ versus λ for different values of j , as $1 \leq j < \infty$. It appears clearly that for $j = 1$, there is only one maximum at $\lambda = 0.5\pi$ for which $\sin(\lambda j) = 1$. For $j = 5$, when $\lambda \in [0, \pi]$, we observe three maxima, and the central one is still situated at $\lambda = 0.5\pi$. Nevertheless, fixing $j = 10$ gives rise to an explosion of maxima where the nearest ones to $\lambda = 0.5\pi$ are $\lambda_1 = 0.45\pi$ and $\lambda_2 = 0.65\pi$. Equivalently, $\sin(qj)$ is expected to display

Table 1

Model parameters for analytical and numerical analyses.

Parameter	Value
k_f	1.0 s^{-1}
k_2	$1.0 \text{ }\mu\text{m}$
k_a	$0.9 \text{ }\mu\text{m}$
k_r	$2.0 \text{ }\mu\text{m}$
V_0	$1.3 \text{ }\mu\text{m s}^{-1}$
V_1	$7.3 \text{ }\mu\text{m s}^{-1}$
V_{m2}	$65.0 \text{ }\mu\text{m s}^{-1}$
V_{m3}	$500.0 \text{ }\mu\text{m s}^{-1}$
β	0.40

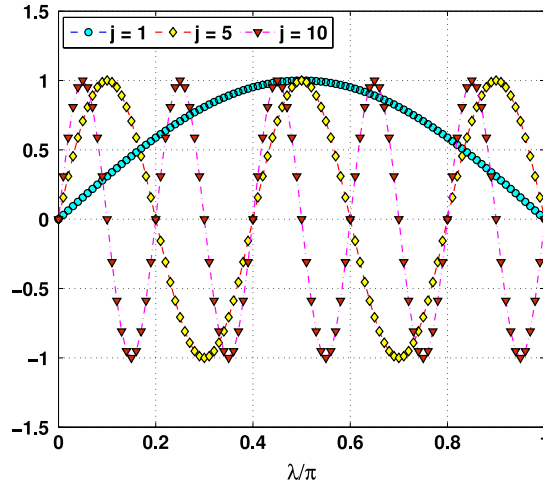


Fig. 3. Representation of $\sin(\lambda j)$ for different values of j . The possible value of λ which gives the highest value of the critical amplitude depends on the long-range character of the system and change with j .

the same behaviors. However, for simplicity, and since the problem at hand is a boundary-condition one, we will consider $\sin(\lambda j) = 1$, which straightforwardly implies the emergence of unstable patterns of CaWs if

$$R/Q < 0 \quad \text{and} \quad |\eta_0|^2 > \frac{2k_0}{R} \sum_{j=1}^{\infty} |j|^{-s} \sin(qj) = \eta_{0,cr}^2. \quad (23)$$

Along the same line, if $R/Q > 0$, there will be MI if $|\eta_0| > |\eta_{0,cr}|$. When these conditions are not satisfied, the plane wave is said to be stable under modulation and flow across the cell lattice without any distortion. In Fig. 4, the critical amplitude is displayed versus the wavenumber q , when N , the number of cells that feel the LRI effects, increases. In these figures, we should precise that $\eta_{0,cr}$ is calculated numerically, while the sum on j is restricted to the interval $j \in [1, N]$. The following features of instability are then obvious:

- for $N = 5$, interactions are felt up to the fifth neighbors and the critical amplitude shows the existence of an unstable region displayed by I, while stable regions are indicated by S. The instability region, whose maximum is $\eta_{0,cr} = 0.025 \text{ }\mu\text{M}$ is situated in the interval $0 < q < q_{cr}$, with $q_{cr} = 0.4\pi$. In that particular region, patterns of CaWs are expected while in other regions the plane wave will be said to be stable.
- For $N = 10$, the LRI spans among the first tenth neighbors and this brings about modifications in the instability features. In panel (b) of Fig. 4, we clearly see how the unique unstable region has splitted into two regions of instability, indicated by I. The plane wave will then be unstable for $0 < q < q_{1,cr}$ ($q_{1,cr} = 0.2\pi$) and for $0 < q < q_{2,cr}$ ($q_{2,cr} = 0.4\pi$). Therefore, the unstable regions are highly sensitive to the number of cells that simultaneously interact in the lattice, as one sees an explosion of unstable domains with increasing N .

Another factor which has been shown to be of deep importance in this modified model is s , for which specific values correspond to different types of long-range interactions. For instance, one should remember that for $s \rightarrow \infty$, the nearest-neighbor features are expected to be recovered. Also, in order to qualitatively see the effect of the length of the lattice neighbor j , we have plotted, in Fig. 5(a), $\eta_{0,cr}$ versus j . For that particular case, we have fixed $N = 5$, and for $s = 1$, the highest value for $\eta_{0,cr}$ belongs to the interval $1 < j < 2$. Also in this case, we observe instability sidebands situated in the intervals $4 < j < 6$ and $8 < j < 10$, which progressively disappear with increasing s , as one can see for $s = 5$ and $s = 20$,

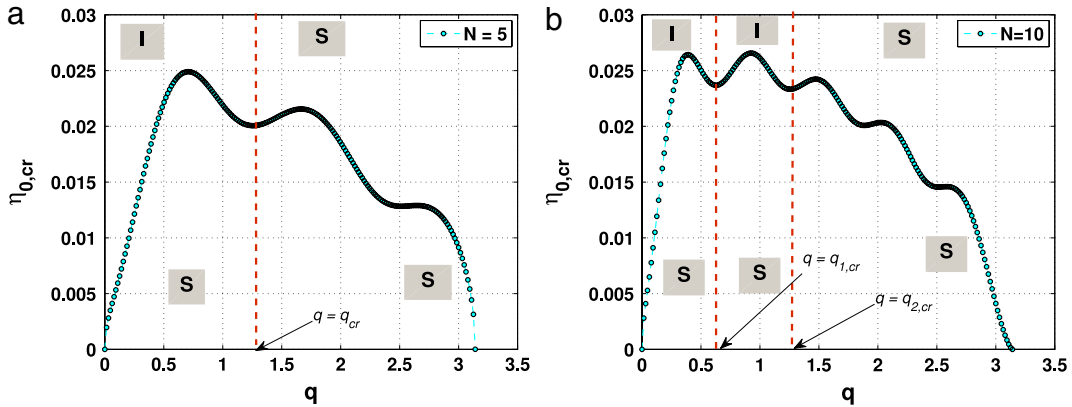


Fig. 4. The panels show the critical amplitude $\eta_{0,cr}$ versus the wavenumber q . In panel (a) the number of interacting cells has been considered to be $N = 5$, while in panel (b), it has been extended to $N = 10$. The stability regions are indicated by (S) while the instability regions are denoted by (I).

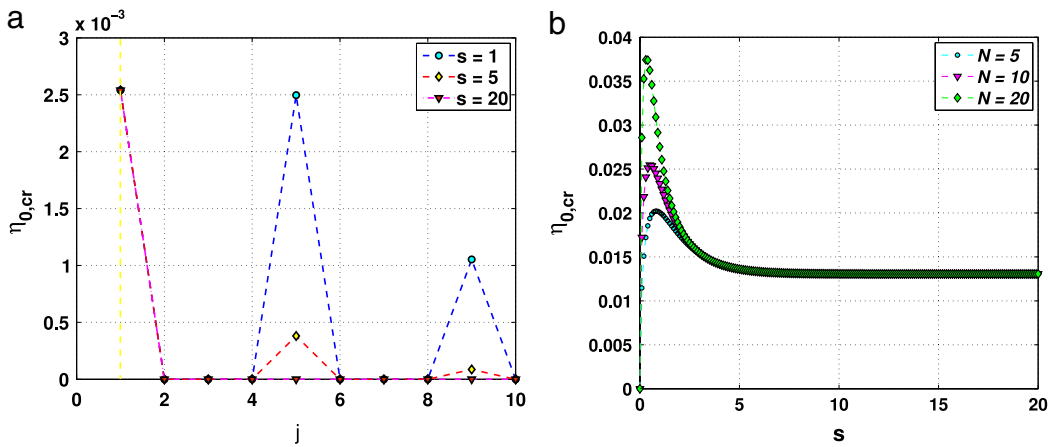


Fig. 5. The figure shows: (a) the representation of $\eta_{0,cr}$ versus j and (b) the plot of $\eta_{0,cr}$ versus s . In the first panel (a), we have fixed $N = 10$, and for $s = 1$, the highest value for $\eta_{0,cr}$ belongs to the interval $1 < j < 2$. Also in this case, we observe instability sidebands situated in the intervals $4 < j < 6$ and $8 < j < 10$, which progressively disappear with increasing s , as one can see for $s = 5$ and $s = 20$, thus confirming the possibility of cell lattice to switch from long-range to nearest-neighbors interactions. In Panel (b), the same features are ostensible, showing that even with increasing N , only small values of s can give rise to long-range intercellular communications.

thus confirming the possibility of cell lattice to switch from long-range to nearest-neighbor interactions. The same features are ostensible in Fig. 5(b), where $\eta_{0,cr}$ has been plotted versus s , showing that even with increasing N , only small values of s can give rise to long-range intercellular communications.

3.2. Numerical results

From the asymptotic expansion to the linear stability analysis, simplifications have been brought to the set of Eqs. (1) to make them more mathematically manipulable. Particularly, the linear stability analysis being based on the linearization around the unperturbed wave, it only gives information about the onset of MI and cannot say anything on the longtime evolution of eventual nonlinear localized structures. On this background, we have integrated the set of Eqs. (1) through the fourth-order Runge–Kutta computational technique for a lattice of 500 cells with periodic boundary conditions. A time-step $\Delta t = 10^{-3}$ has been used and initial conditions have been introduced as slightly modulated waves.

3.2.1. Stable plane waves of Ca^{2+}

Before going through the study of unstable patterns of CaWs, we first check numerically the validity of our stability condition. In this framework, the simulations of Fig. 6 have been done using $\eta_0 = 0.2$. Wavenumbers have been chosen in the stable region of Fig. 4 and only the cytosolic calcium dynamics has been considered. Therefore, for $q = 0.55\pi$ and $\lambda = 0.4\pi$, Fig. 6(a) and (b) indeed correspond to the predicted stable cases. All the parameters here are the same, excepted that the features of the plane wave change with increasing the range parameter s . In fact, due to the strength of the long-range effects, i.e., small values of s , the wavelength of the plane wave is high and pictures a sort of continuous wave, as displayed by

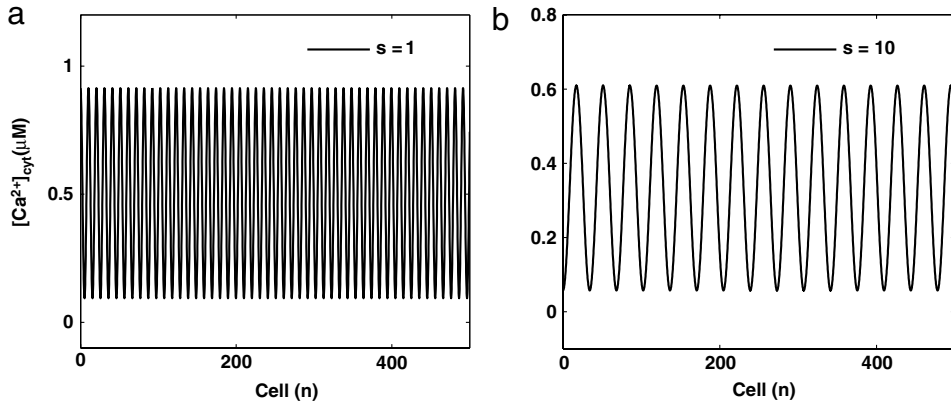


Fig. 6. Modulational stability of Ca^{2+} waves for different values of the range parameter s , at time $t = 2000$ s. In panel (a), $s = 1$, the strength of the long-range coupling gives rise to long-wavelength plane wave, while increasing the range parameter to $s = 10$ reduces the wavelength of the plane wave. Parameters have been chosen in the region of stability as $q = 0.55\pi$ and $\lambda = 0.45\pi$.

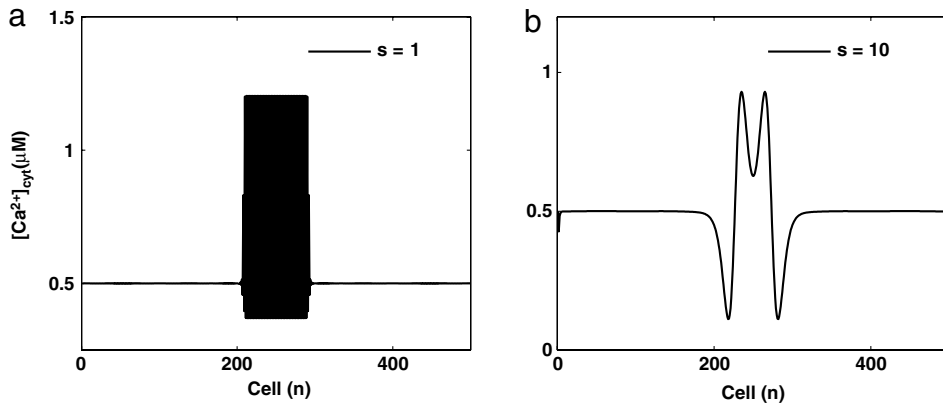


Fig. 7. MI of a plane wave leading to the formation of a single soliton-like object for $q = 0.25\pi$ and $\lambda = 0.15\pi$. Panels (a) and (b) have been plotted at time $t = 2000$ s, for $s = 1$ and $s = 10$, respectively.

Fig. 6(a), where $s = 1$. On the other hand, large values of s , e.g., $s = 10$, reduce the wavelength, therefore exposing individual oscillations of the plane wave patterns (see Fig. 6(b)). The comportment of these stable plane waves under long-range could then predict how it will be for the case of MI. One thing to also be noticed is the decrease of the plane wave amplitude with increasing s , which could bring about important implications on intercellular communication.

3.2.2. Unstable wave patterns of Ca^{2+}

In order to have a look at MI, we have first restricted ourselves to the region of instability where only one solitonic object can be observed. The results observed in Fig. 7, for $\eta_0 = 0.4$, $q = 0.25\pi$ and $\lambda = 0.15\pi$, are in good agreement with our analytical predictions, as one can clearly recognize a breathing-like structure for $s = 1$. Interestingly, the wavelength of oscillations reduces with increasing the range parameter s to 10. As previously, the real effect of long-range interactions is to increase the wavelength of spatial Ca^{2+} oscillations, and this could picture a better cell–cell communication.

Although some regions of parameters can give rise to the behaviors of Fig. 7, the main characteristics of MI is that the plane wave usually breaks into trains of wave packets with solitonic profile. Also, the case of Fig. 7 just restricts interactions to a small agglomeration of cells, whereas we suppose the network to be made of several entities. For the dynamics of the whole lattice to be therefore viewed, we have picked the point corresponding to the wavenumbers $q = 0.45\pi$ and $\lambda = 0.35\pi$, with $\eta_0 = 0.4$ as previously. Satisfactorily, CaWs display oscillating and breathing wave behaviors. Also, it is found that the applied wavenumbers influence the number of patterns oscillating with solitonic shape. However, the range parameter plays on the modulation of these structures, as the wavelength decreases with increasing s , as clearly depicted in Fig. 8(a)–(d), for $s = 1, 3, 5$ and 10 respectively. This is in agreement with the previous cases, even for stable plane waves, where the same phenomenon has been observed. Importantly, when s increases, the LRI drops and advantage is given to first-neighbor interactions, leading to a modification in the spatial expansion of the formed CaWs. Consequently, as the range

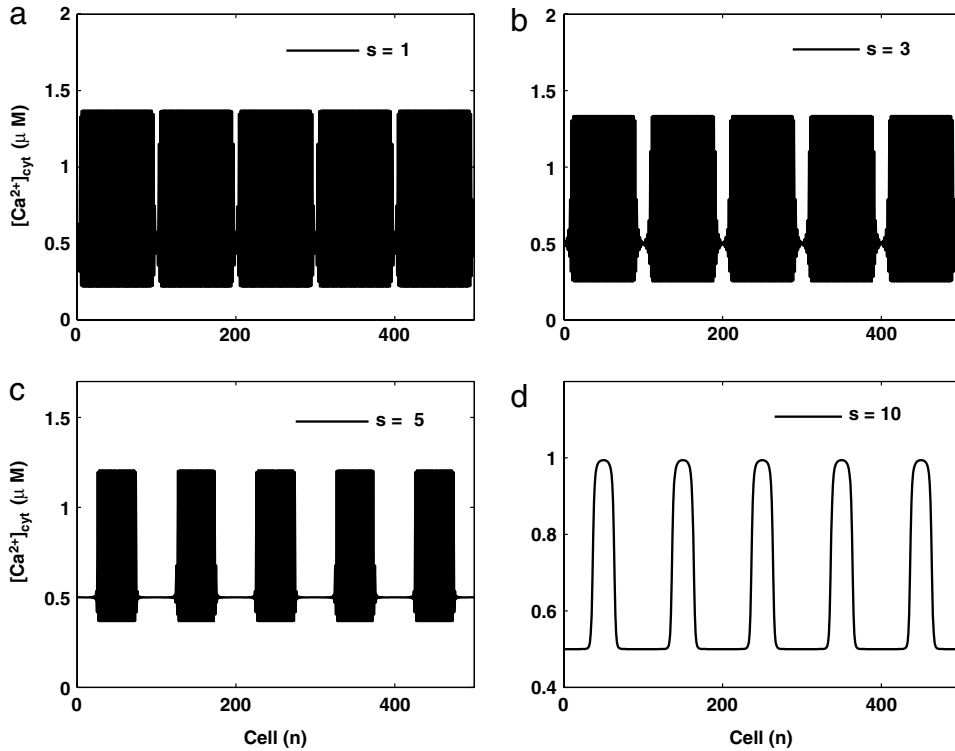


Fig. 8. Modulational instability of Ca^{2+} waves for different values of the range parameter s , at time $t = 2000$ s. (a) $s = 1$, the intercellular communication is characterized by train of soliton-like objects with ultrashort wavelength and breathing features. (b) For $s = 3$, unstable wave patterns still develop as trains of breathers-like structures, with short wavelength, therefore reducing the spatial expansion of the individual waves. Increasing the range parameter s therefore has the effect of increasing the wavelength of the breathing objects and is shown to restrict intercellular communication to some range of cells as it is further confirmed by panel (c), where $s = 5$. For very large values of s , the long-range effect is expected to vanish and the system to behave accordingly. This is illustrated via impulses that show no modulation, but still appear as trains of soliton-like objects as shown in panel (d) where we have fixed $s = 10$.

parameter reveals itself to contribute in changing the characteristics of the obtained wave trains, we have further increased its value up to $s = 10$ and we have obtained the behaviors of Fig. 8(d), which clearly shows that pulse-like trains of waves can emerge in such models. As our system is a spatially extended dynamical system with large numbers of degrees of freedom (the individual cells), such systems are always expected to manifest complex spatiotemporal behaviors when parameters are modified or when, in our context, wavenumbers are picked from different unstable regions. In order to get an insight into the spatiotemporal evolution of the formed patterns, we have further played on value of s , and we have qualitatively evaluated the effect of LRI on CaWs propagation. Therefore, in the first panel of Fig. 9, the quasi-perfect intercellular communication is materialized by connected bands of Ca^{2+} patterns. The LRI obviously enhances efficient information transfer among coupled cells, therefore leading to long-range signaling within the brain, for example.

Behaviors as those of Fig. 9(a) have been observed in Ref. [12], where we brought out the effect of the paracrine coupling parameter. The latter was fixed to be $\beta = 0.6$ for these behaviors to be observed, while for the case of Fig. 9(a), we have taken it as $\beta = 0.3$. The obtained quasi-linear structures display zigzag connected CaW patterns which show modification in the way cells interact in the lattice. However, from $t = 0$, the sequences of interconnected cells are apparent, albeit they tend to form linear patterns as time increases. Still, we do not change the value of the paracrine coupling constant, but as s increases, we expect the formed patterns to change their features as this is the case for Fig. 9(b), where we have fixed $s = 5$. The coherent features observed in the previous case are affected as zig-zag patterns are now more visible. In the case LRI is no more effective in the system, there will however remain sequences of interacting cells as shown in Fig. 9(c), where $s = 10$. In order to complete the present analysis, we have plotted the temporal evolution of CaWs in some individual cells for $s = 1$. Remarkably, series of spikes are obtained, and their behaviors clearly picture long-range effects. We clearly notice that cells 50 (Fig. 10(a)) and 450 (Fig. 10(d)) display the same dynamics, while cells 200 (Fig. 10(b)) and 300 (Fig. 10(c)) also oscillate the same way.

4. Discussion and conclusion

In this study, the propagation of CaWs via the activation of MI, in presence of long-range dispersive effects, is examined. The release of Ca^{2+} in the extracellular medium is responsible for the so-called paracrine signaling, which is not restricted

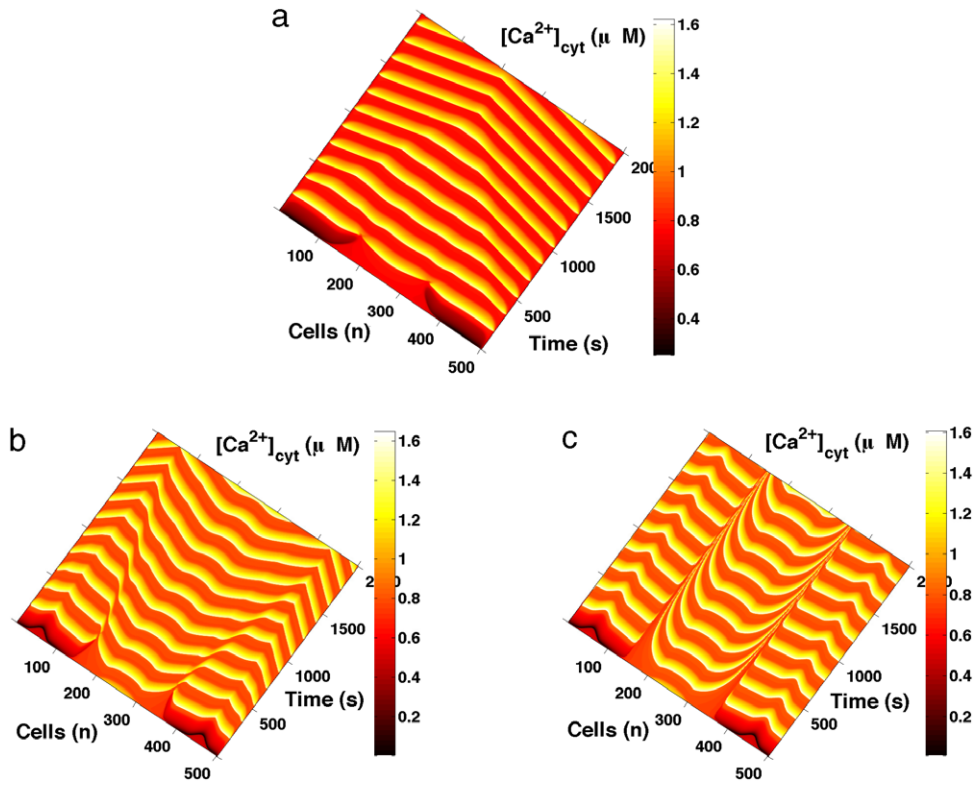


Fig. 9. Spatiotemporal patterns of the cytosolic Ca^{2+} oscillations for $N = 5$, $\beta = 0.4$ and (a) $s = 1$, (b) $s = 5$ and (c) $s = 10$. In the first panel, the patterns form three large spatial rows which include large sequences of communicating cells. Many cells are therefore involved in the long-range cell–cell communication, while the individual rows get interconnected with increasing the coupling parameter β , then forming large bands of Ca^{2+} patterns as shown in panel (b).

to only nearest-neighbor cells. It is proposed that MI could be responsible for information sharing among interconnected cells via modulated wave patterns as interestingly presented in this paper. As a consequence of the interplay between nonlinear and dispersive effects, such structures are actually popular in biological systems, where they play various roles for specific purposes. In that respect, amplitude and frequency modulated waves were observed in spatially extended astrocytes [28], i.e., Ca^{2+} excitations evoked in individual astrocytes could spread throughout neighboring cells, with strong implications of linear and nonlinear couplings. Along the same line, the present contribution suggests that long-range coupling could be perceived as a way to encode information for specific processes to be controlled. Specifically, astrocytes communicate with each other and even cooperate with distant neurons, as facilitated by LRI [29]. Extended modulated waves can therefore be viewed as a materialization of distant interactions, where the synaptic release of glutamate [30], GABA [31], noradrenaline [32] and acetylcholine [33] is of deep importance. These substances and messengers, released in the extracellular space, enhance intercellular communication and even provide a probable route for long-distance propagation of CaWs, whose reception depends on the activation of calcium-sensing receptors (CaRs). The density of activated CaRs could therefore be responsible for the efficiency and strength of long-range CaWs spreading. On that view, hyperactivation of astrocytes could be a good example due to the formation of new synapses, and then chronic pain, as a consequence of self-sustained and long-distance Ca^{2+} patterns in astrocyte networks [34]. A phenomenon that is straightly linked to the formation of these new synapses is epilepsy [35], which can be avoided if the quantity of glutamate is controlled, which influences the qualitative characteristics of modulated CaWs by controlling the strength of long-range effects.

To summarize, we have used MI both analytically and numerically to show that LRI can be at the basis of a quasi-perfect cell–cell communication. The long-range dispersive coupling have been shown to bring about new features in the emergence of localized Ca^{2+} structures. We have therefore obtained extended breather-like modes for strong coupling while increasing the range parameter has been shown to reduce the wavelength of the formed modulated waves. Finally, trains of pulse-like waves have been obtained for $s \rightarrow +\infty$, then reducing the problem to the first-neighbor one. Otherwise, the LRI plays an important role in the way information flow in the cell array and could even favor the spreading of toxins as cells get progressively infected, colonized by infected ones. However, we should stress that the proposed model does not include IP_3 effect, which deserves to be deeply regarded. There are ongoing work in that direction.

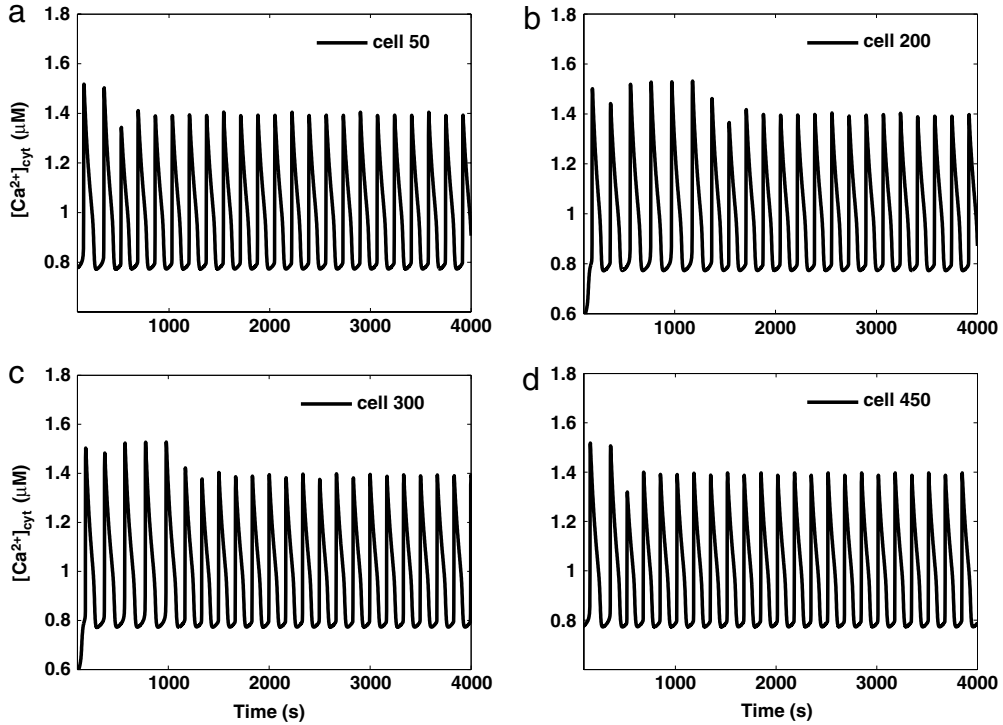


Fig. 10. Temporal evolution of Ca^{2+} oscillations of the cell: (a) $n = 50$, (b) $n = 200$, (c) $n = 300$ and (d) $n = 450$. The dynamical behaviors of these individual cells are compared under strong long-range effects, i.e., $s = 1$. Cells 50 and 450 display almost the dynamics, while cells 200 and 300 have similar oscillatory behaviors. Strong long-range coupling is responsible for bringing sequences of cells to behave the same way. Parameters are the same as in Fig. 7.

Acknowledgments

CBT acknowledges the Claude Leon Foundation for research fellowship at Stellenbosch University, South Africa. Prof. K.K. Müller-Nedebock is also acknowledged for fruitful suggestions.

Appendix A. The leading order (1, l)

$$\begin{aligned} \sum_{l=-1}^1 i l \Omega \psi_1^{(l)}(m, \tau) A^{(l)} &= \sum_{l=-1}^1 \sum_{j=1}^{\infty} k_0 |j|^{-s} 2(\cos(qjl) - 1) \psi_1^{(l)}(m, \tau) A^{(l)} + k_f \sum_{l=-1}^1 \phi_1^{(l)}(m, \tau) A^{(l)} - k \sum_{l=-1}^1 \psi_1^{(l)}(m, \tau) A^{(l)} \\ \sum_{l=-1}^1 i l \Omega \phi_1^{(l)}(m, \tau) A^{(l)} &= -k_f \sum_{l=-1}^1 \phi_1^{(l)}(m, \tau) A^{(l)}. \end{aligned} \quad (24)$$

Appendix B. The order (2, l)

$$\begin{aligned} \sum_{l=-1}^1 \frac{\partial}{\partial \tau} \psi_1^{(l)}(m, \tau) A^{(l)} + \sum_{l=-2}^2 i l \Omega \psi_2^{(l)}(m, \tau) A^{(l)} &= \sum_{l=-1}^1 \sum_{j=1}^{\infty} k_0 |j|^{-s} \left(\frac{2ij}{v_g} \right) \sin(qjl) \frac{\partial}{\partial \tau} \psi_1^{(l)}(m, \tau) A^{(l)} \\ &+ \sum_{l=-2}^2 \sum_{j=1}^{\infty} k_0 |j|^{-s} 2(\cos(qjl) - 1) \psi_2^{(l)}(m, \tau) A^{(l)} + \left(\frac{V_0}{k_2^2} - \alpha_3 \right) \left(\sum_{l=-1}^1 \psi_1^{(l)}(m, \tau) A^{(l)} \right)^2 \\ &+ k_f \sum_{l=-2}^2 \phi_2^{(l)}(m, \tau) A^{(l)} - k \sum_{l=-2}^2 \psi_2^{(l)}(m, \tau) A^{(l)} + \frac{V_0}{k_r^2} \left(\sum_{l=-1}^1 \phi_1^{(l)}(m, \tau) A^{(l)} \right)^2 \\ \sum_{l=-1}^1 \frac{\partial}{\partial \tau} \phi_1^{(l)}(m, \tau) A^{(l)} + \sum_{l=-2}^2 i l \Omega \phi_2^{(l)}(m, \tau) A^{(l)} &= \alpha_3 \sum_{l=-2}^2 \phi_2^{(l)}(m, \tau) A^{(l)} - k_f \left(\sum_{l=-1}^1 \psi_1^{(l)}(m, \tau) A^{(l)} \right)^2. \end{aligned} \quad (25)$$

Appendix C. The order (3, l)

$$\begin{aligned}
& \sum_{l=-2}^2 \frac{\partial \psi_2^{(l)}}{\partial \tau} A^{(l)} + \sum_{l=-3}^3 i l \Omega \psi_3^{(l)} A^{(l)} - \sum_{l=-1}^1 \sum_{j=1}^{\infty} k_0 |j|^{-s} \left(\frac{j}{v_g} \right)^2 \cos(qjl) \frac{\partial^2}{\partial \tau^2} \psi_1^{(l)}(m, \tau) A^{(l)} \\
& - \sum_{l=-1}^1 \sum_{j=1}^{\infty} k_0 |j|^{-s} i \sin(qjl) \left(\psi_1^{(l)}(m+j, \tau) - \psi_1^{(l)}(m-j, \tau) \right) A^{(l)} \\
& - \sum_{l=-2}^2 \sum_{j=1}^{\infty} k_0 |j|^{-s} \left(\frac{2ij}{v_g} \right) \sin(qjl) \frac{\partial}{\partial \tau} \psi_2^{(l)}(m, \tau) A^{(l)} - \sum_{l=-3}^3 \sum_{j=1}^{\infty} k_0 |j|^{-s} 2(\cos qjl - 1) \psi_3^{(l)}(m, \tau) A^{(l)} \\
& - \alpha_1 \sum_{j=1}^{\infty} k_0 |j|^{-s} \left(\sum_{l=-1}^1 2(\cos(qjl) - 1) \psi_1^{(l)}(m, \tau) A^{(l)} \right) \left(\sum_{l=-1}^1 \phi_1^{(l)}(m, \tau) A^{(l)} \right)^2 \\
& - \alpha_2 \sum_{j=1}^{\infty} k_0 |j|^{-s} \left(\sum_{l=-1}^1 2(\cos(qjl) - 1) \psi_1^{(l)}(m, \tau) A^{(l)} \right) \left(\sum_{l=-1}^1 \psi_1^{(l)}(m, \tau) A^{(l)} \right)^2 \\
& - k_f \sum_{l=-3}^3 \phi_3^{(l)} A^{(l)} - k \sum_{l=-3}^3 \psi_3^{(l)} A^{(l)} - 2 \left(\frac{V_0}{k_2^2} - 2\alpha_3 \right) \left(\sum_{l=-1}^1 \psi_1^{(l)}(m, \tau) A^{(l)} \right) \left(\sum_{l=-2}^2 \psi_2^{(l)}(m, \tau) A^{(l)} \right) \\
& + \gamma_2 \left(\sum_{l=-1}^1 \psi_1^{(l)} A^{(l)} \right) \left(\sum_{l=-1}^1 \phi_1^{(l)} A^{(l)} \right)^2 + \gamma_1 \left(\sum_{l=-1}^1 \psi_1^{(l)} A^{(l)} \right)^3 - \beta_1 \left(\sum_{l=-1}^1 \phi_1^{(l)} A^{(l)} \right)^3 \\
& - \beta_2 \left(\sum_{l=-1}^1 \phi_1^{(l)} A^{(l)} \right) \left(\sum_{l=-1}^1 \psi_1^{(l)} A^{(l)} \right)^2 - \frac{2V_0}{k_r^2} \left(\sum_{l=-1}^1 \phi_1^{(l)}(m, \tau) A^{(l)} \right) \left(\sum_{l=-2}^2 \phi_2^{(l)}(m, \tau) A^{(l)} \right) = 0 \\
& \sum_{l=-2}^2 \frac{\partial \phi_2^{(l)}}{\partial \tau} A^{(l)} + \sum_{l=-3}^3 i l \Omega \phi_3^{(l)} A^{(l)} - 2\alpha_3 \left(\sum_{l=-1}^1 \psi_1^{(l)}(m, \tau) A^{(l)} \right) \left(\sum_{l=-2}^2 \psi_2^{(l)}(m, \tau) A^{(l)} \right) \\
& + \beta_1 \left(\sum_{l=-1}^1 \phi_1^{(l)} A^{(l)} \right)^3 - \beta_2 \left(\sum_{l=-1}^1 \phi_1^{(l)} A^{(l)} \right) \left(\sum_{l=-1}^1 \psi_1^{(l)} A^{(l)} \right)^2 + k_f \sum_{l=-3}^3 \phi_3^{(l)} A^{(l)} = 0.
\end{aligned} \tag{26}$$

References

- [1] E.R. Kandel, J.H. Schwartz, T.M. Jessel, *Principles of Neural Science*, Appleton and Lange, Norwalk, 1991.
- [2] M.J. Berridge, M.D. Bootman, P. Lipp, *Nature* 395 (1998) 645.
- [3] M. Wilkins, J. Sneyd, *J. Theoret. Biol.* 191 (1998) 299.
- [4] U. Kummer, L.F. Olsen, C.J. Dixon, A.K. Green, E. Bornberg-Bauer, G. Baier, *Biophys. J.* 79 (2000) 1188.
- [5] T. Höfer, A. Politi, R. Heinrich, *Biophys. J.* 80 (2001) 75.
- [6] G. Dupont, Th. Tordjmann, C. Clair, St. Swillens, M. Claret, L. Combettes, *FASEB J.* 14 (2000) 279.
- [7] T.D. Hassinger, P.B. Guthrie, P.B. Atkinson, M.V. Bennett, S.B. Kater, *Proc. Natl. Acad. Sci. USA* 93 (1996) 13268.
- [8] J. Sneyd, A.C. Charles, M.J. Sanderson, *Am. J. Physiol. Cell. Physiol.* 266 (1994) C293.
- [9] M.H. Nathanson, A.D. Burgstahler, A. Mennone, M.B. Fallon, C.B. Gonzalez, J.C. Saez, *Am. J. Physiol.* 269 (1995) G167.
- [10] M.E. Gracheva, J.D. Gunton, *J. Theoret. Biol.* 221 (2003) 51.
- [11] W.D. Kepseu, P. Wofo, *Phys. Rev. E* 73 (2006) 041912.
- [12] C.B. Tabi, I. Maïna, A. Mohamadou, H.P.F. Ekobena, T.C. Kofané, *Europhys. Lett.* 106 (2014) 18005.
- [13] V.E. Zakharov, L.A. Ostrovsky, *Physica D* 238 (2009) 540.
- [14] A. Mohamadou, B.E. Ayissi, T.C. Kofané, *Phys. Rev. E* 74 (2006) 046604.
- [15] T.B. Benjamin, J.E. Feir, *J. Fluid Mech.* 27 (1967) 417.
- [16] A.D. Koko, C.B. Tabi, H.P.F. Ekobena, A. Mohamadou, T.C. Kofané, *Chaos* 22 (2012) 043110.
- [17] C.B. Tabi, A. Mohamadou, T.C. Kofané, *J. Phys.: Condens. Matter* 21 (2009) 335101.
- [18] G.R.Y. Mefire, C.B. Tabi, A. Mohamadou, H.P.F. Ekobena, T.C. Kofané, *Chaos* 23 (2013) 033128.
- [19] C.B. Tabi, J.C.F. Mimshe, H.P.F. Ekobena, A. Mohamadou, T.C. Kofané, *Eur. Phys. J. B* 86 (2013) 374.
- [20] E. Wamba, A. Mohamadou, T.C. Kofané, *Phys. Rev. E* 77 (2008) 046216.
- [21] B.E. Isakson, W.H. Evans, S. Boitano, *Am. J. Physiol.* 280 (2001) L221.
- [22] Y. Osipchuk, M. Cahalan, *Nature* 359 (1992) 241.
- [23] M.K. Frame, A.W. De Feijter, *Exp. Cell Res.* 230 (1997) 197.
- [24] A. Goldbeter, G. Dupont, M.J. Berridge, *Proc. Natl. Acad. Sci. USA* 87 (1990) 1461.
- [25] B.M. Shaffer, *Nature* 79 (1953) 975.
- [26] J. Leon, M. Manna, *Phys. Rev. Lett.* 83 (1999) 2324.
- [27] C.B. Tabi, A. Mohamadou, T.C. Kofané, *Chaos* 19 (2009) 043101.
- [28] M. Takeda, D.J. Nelson, B. Soliven, *Glia* 14 (1995) 225.

- [29] C. Giaume, L. Venance, Characterization and regulation of gap junction channels in cultured astrocytes, in: D.C. Spray, R. Dermietzel (Eds.), *Gap Junctions in the Nervous System*, R.G. Landes Company, 1996, pp. 135–157.
- [30] J.T. Porter, K.D. McCarthy, *J. Neurosci.* 16 (1996) 5073.
- [31] J. Kang, L. Jiang, S.A. Goldman, M. Nedergaard, *Nat. Neurosci.* 1 (1998) 683.
- [32] A. Kulik, A. Haentzsch, M. Luckermann, W. Reichelt, K. Ballanyi, *J. Neurosci.* 19 (1999) 8401.
- [33] M. Navarrete, G. Perea, D.F. de Sevilla, M. Gomez-Gonzalo, A. Nunez, E.D. Martin, A. Araque, *PLoS Biol.* 10 (2012) e1001259.
- [34] E. Hansson, *Acta Physiol. (Oxf.)* 187 (2006) 321.
- [35] G.-F. Tian, H. Azmi, T. Takano, Q. Xu, W. Peng, J. Lin, N.A. Oberheim, N. Lou, R. Zeilke, R. Kang, M. Nedergaard, *Nat. Med.* 11 (2005) 973.